RSC Advances

ROYAL SOCIETY OF CHEMISTRY

www.rsc.org/advances

Journal Name

RSCPublishing

ARTICLE

Superparamagnetic amorphous iron oxide nanowires self-assembled into ordered layered structures

Cite this: DOI: 10.1039/x0xx00000x

M. Iacob,[a,b] D. Sirbu,[b] C. Tugui[a], G. Stiubianu,[a] L. Sacarescu,[a] V. Cozan,[a] A. Zeleňáková,[c] E. Čižmár,[c] A. Feher,[c] and M. Cazacu[a]

Received ooth January 2012,
Accepted ooth January 2012

DOI: 10.1039/x0xx00000x

www.rsc.org/

The thermal decomposition of μ3-oxo trinuclear iron(III) acetate in presence of dodecylamine and oleic acid, in thricloroacetic acid at 320 ˚C was optimized to obtain iron oxide nanoparticles with pure nanowire morphology. The amount of oleic acid having a surfactant role, beside the ligand exchange for acetate, was used as a control parameter. The size and morphology of the resulted particles were evaluated on the basis of transmission electron microscopy images. Thermal stability and the content of the organic component of the naoparticles were determined by thermogravimetrical analysis. The ordering degree of the organic and inorganic phases constituting the nanoparticles was investigated by wide angle X-Ray diffraction, small angle X-ray scattering and polarized optical microscopy. Superparamagnetic state was verified by Mössbauer spectroscopy and the magnetic behavior was studied by SQUID magnetometry. The preservation of the morphology of the particles after complete thermal decomposition was verified by transmission electron microscopy.

Introduction

Magnetic particles are materials very useful in a wide range of applications, such as magnetic resonance images (MRI) contrast agents and hyperthermia agents.[1,2] Iron oxides are one of the most commonly used and well-studied magnetic materials. But, as it is known, the magnetic properties are highly dependent on the size, shape and structure of the particles. While the properties of the materials change dramatically from bulk to the nanometer scale, the control of the morphology of the nanoparticles at this level is one of the most important missions in nanotechnology. Iron oxides are among the most studied materials due to their fundamental properties and potential applications. One-dimensional (1-D) iron oxides nanostructures became of high interest in the last decades because of their wide applications in magnetic refrigeration, electronics, catalysts, Li-ion batteries, pigments, gas sensors, etc.[3] Due to their nano-scale one-dimensional structure, nanowire shape, one of the possible morphologies, shows unique mechanical, electrical, magnetic properties having potential applications for various mesoscopic electronic and optical devices.[4,5] Due to their large aspect ratios resulting in high surface areas, the nanowire morphology is attractive for sensors and detectors. It has been shown that the magnetorheological (MR) performance of nanowire fluid is better than that of spherical particle fluid, in terms of yield stress, compression displacement, and creep recovery ratio.[6] Many scientists pursued the goal of producing metal-oxide nanowires such as β-Ga_2O_3, SiO_2, In_2O_3, ZnO, SnO_2 for use in all the areas of technology. But only a few reports dealing with the production of iron oxide nanowires can be found at present, especially ones that use affordable chemical routes.[7] The research for the production of iron oxide nanowires has both theoretical and practical interest because these could be useful in a variety of fields, such as in medicine[8], as biological and magnetic contrast[9], as starting material for the preparation of photoconductors,[10] in biology,[11] in catalysis of carbon nanotube growth.[12] Mohaparta et al.[13] in 2015 reported enhanced MRI contrast of iron oxide nanorods that was attributed to the higher surface area and anisotropic morphology. The higher surface area induces a stronger magnetic field perturbation over a larger volume more effectively for the outer sphere protons. The induced magnetic field of nanorods is stronger than that of spherical particles and the stronger magnetic field over a large volume leads to a higher R_2 relaxivity of nanorods. Iron oxide, Fe_2O_3, has very good thermal stability and can impart UV protection when introduced in polymer matrixes used in various commercial products.[14] Various strategies were used for the preparation of iron oxide nanowires. Thus, Fu et al.[15] prepared nanowires of Fe_2O_3 (15-75 nm width x 10-20 μm length) by oxygenating pure iron. Another procedure uses the action of nitrilotriacetic acid (NTA) as a chelating agent to form polymeric chains by hydrothermal method with $FeCl_3$ as iron source, leading to α-Fe_2O_3 nanowires with lengths of tens of micrometres and up to 120 nm width.[16] Iron-oxide nanowires with 10–15 nm in diameter and 600 nm in length were synthesized by a

hydrothermal treatment of $Fe(OH)_3$ dispersion in NaOH, the structural and magnetic investigations revealing formation of goethite.[17] Iron oxide nanowires were also prepared directly from iron foils through the simple heating in normal atmosphere.[18] Quasi-circular Fe_3O_4 nanoparticles synthesized by co-precipitation method were subsequently converted in nanowires at high temperature and high pressure in a strongly alkaline environment.[6] Iron oxide as tubes and fibrils nanoparticles were grown within the pores of nanoporous polycarbonate and alumina membranes by hydrolysis and polymerization of iron salts or by the sol-gel technique, using metallo-organic compounds as reagents.[19] The photochemical method through nanosecond pulsed laser (248 nm) ablation of iron powder (size < 60 μm) in liquids (methanol) media leads also to iron oxide nanowires.[20]

Unlike the routes used in the above mentioned studies, in this paper we present an efficient path for preparation of amorphous iron oxide nanowires by one-step method of thermal decomposition using μ3-oxo trinuclear iron(III) acetate as precursor, dodecylamine, oleic acid and thricloroacetic acid in an appropriate ratio. The composition, properties and behaviour of the nanowires were determined by spectral method (FTIR, SAXS, XRD, and Mössbauer), microscopy (TEM), thermal methods (TGA, DSC), POM and SQUID magnetometry in order to have a clear image of this material's properties for future possible uses.

Results and discussion

The well-known thermal decomposition procedure was approached to prepare iron oxide nanoparticles. With this aim, trinuclear iron acetate was used as iron source while oleic acid and docedylamine were added as stabilizing agents and thricloroacetic acid as solvent. It was found that the temperature has an important effect on the growth process and the final morphology of the iron oxide nanoparticles, but oleic acid can also control the size of iron oxide nanoparticles influencing the nucleation rate.[21,22] We conducted a series of syntheses to identify the optimum conditions to obtain nanowire morphology using a certain amount of IA precursor, under the same conditions (constant amounts of dodecylamine and thricloroacetic acid, temperature).

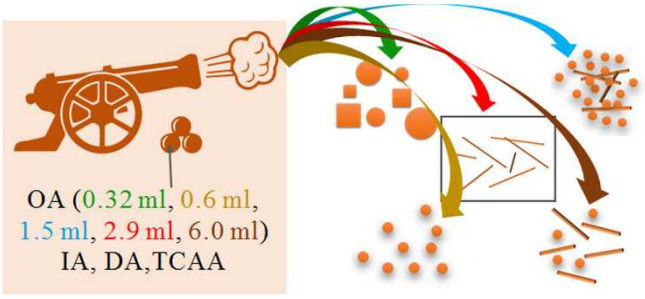

Scheme 1. Graphical representation of the artillery approach for targeting the reaction parameters used in the preparation of NWs

The reactions were carried out one after another, maintaining identical conditions and successively changing only the amount of oleic acid added: 0.32 ml (Figure 1a – NPs1), 0.6 ml (Figure 1b – NPs2), 2.9 ml (Figure 1c – NWs), 1.5 ml (Figure 1d – NPS3), 6 ml (Figure 1e – NPs4). Only adding 2.9 ml oleic acid resulted in the formation of nanowires (Figure 1c – P4c) studied in this report further. Different morphologies resulted for lower or higher amount of oleic acid. For lower volume of oleic acid added to the reaction mixture (from 1.5 ml to 0.32 ml) spherical and cubic polydisperse nanoparticles were obtained (Figure 1a,b). The increased amount up to 6 ml of oleic acid led to a mixture of nanowires and nanoparticles as reaction products (Figure 1e).

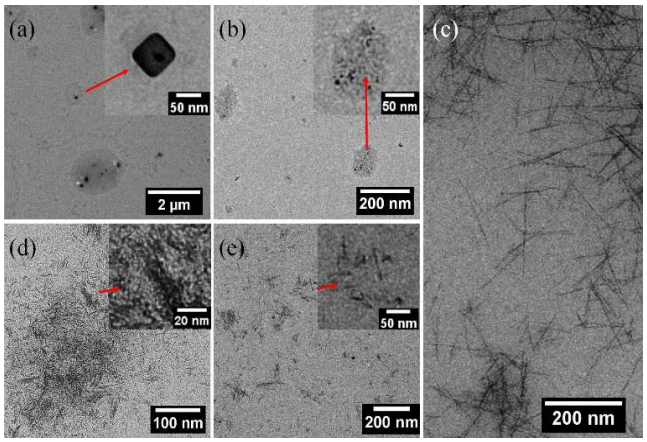

Figure 1. TEM images of NPs 1 (a), NPs2 (b), NWs (c), NPs3 (d) and NPs4 (e)

Iron oxide nanowires were obtained, as mentioned above, by decomposition method using a mixture of iron acetate cluster, oleic acid, dodecylamine and thricloroacetic acid. The reaction took place at 320 ^{o}C in the inert environment. Different processes can take place at such temperature: acetic acid is replaced by oleic acid, decomposition of iron oleate with formation of iron oxides, their clusterization and stabilization.[23,24] It is generally accepted that the key steps in the process of nanoparticles formation are nucleation and growth. According to the classic LaMer theory, the most acceptable mechanism for the formation of the nanoparticles consists in a burst nucleation followed by a diffusional growth to form primary small particles. Then these aggregate into the final particles, the process being determined by the elimination of the repulsive barrier and the diffusion rate of the primary particles which will lead to certain size. However, if nuclei cannot grow at the same time, when the temperature of the polydispersed nanoparticles system is raised, the smaller nanoparticles, due to their high surface energy, progressively dissolve to the benefit of larger ones feeding the growth of them by the so called Ostwald ripening process.[25,26] The main parameters controlling nanowires formation were found to be reaction temperature, concentration and composition of the reactants and stabilizing agents.[27] In our approach, the surfactant concentration was single parameter which was varied. The role of surfactant in nanoparticles nucleation and growth has been observed, for example in the

synthesis of the Co nanoparticles when, in the same system, by varying the surfactant concentration, different nanoparticles growth pathways occur (diffusional growth, aggregation, and Ostwald ripening), leading to various morphologies. On the basis of electronic structure calculations, it has been found that surfactant concentration and its relative bond strength with Co atoms are responsible for resulted morphology.[25] Silver nanostructures with different well-controlled morphologies (e.g., cubes, rods, wires, and spheres) were also obtained by simply tuning the ratio between the capping agent (polyvinylpyrrolidone) and the precursor salt ($AgNO_3$).[28]

The infrared spectrum of the resulted iron oxide nanowires (NWs) as compared with that of iron acetate precursor (IA) are presented in Figure 2. The replacement of the acetate ligand with unsaturated acid is highlighted by the shift of carboxylate bands observed in NWs spectrum (1549 and 1466 cm^{-1}) compared with the one observed in IA spectrum (1600 and 1450 cm^{-1}).[29] The bands characteristic for asymmetrical and symmetrical stretching vibrations of C-H from CH_3 and CH_2 at 2955, 2870 (shoulder) and 2922, 2853, respectively,[30] in the spectrum of NWs indicate the presence of long chain ligand on the nanowires surface (oleic acid and dodecylamine). In addition, the presence of amine group from dodecylamine on nanowires surface is suggested by the bands at 3385, 3318 and 1636 cm^{-1}. The bands in the 720–390 cm^{-1} range of NWs spectrum are typical for Fe-O vibrations[31], from iron oxide core.

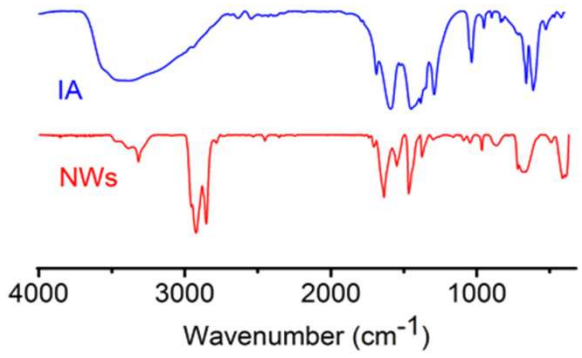

Figure 2. FTIR spectra of the nanowires (NWs) as compared with that for the initial trinuclear acetate (IA)

According to the thermogravimetric analysis results (Figure 3) the NWs compound begins to lose weight around 205 ˚C leaving a residue of 14% at the end of the analysed temperature range. The degradation process occurs in three steps with maxima (from DTGA) at 264 (evaporation of surfactant, mass change 16.3 %), 400.6 and 436 ˚C (decomposition of surfactant, mass change 67.8 %). The high mass loss (86 wt%) in this process is an indication for the large percentage of organic component in the coating of NWs.

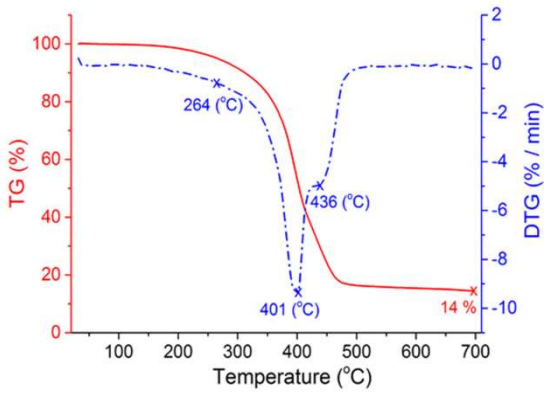

Figure 3. Thermal degradation in nitrogen atmosphere of the iron nanowires

The morphology of NWs was investigated by TEM microscopy showing the nanowires of about 100 nm in length and 3 nm in width (Figure 4). The image with greater magnification (Figure 4b) shows this sample is made only of nanowires, without particles of other shapes. Such pure shape nanowires can be further used for preparation of transparent electrodes, improved dielectric elastomers and particles for medical applications.

Powder WAXD measurements of NWs sample at room temperature have been performed in the region 1.5 – 80˚ 2θ. The wide angle region (30 – 80˚ 2θ) of the diffractogram (Figure S1) does not contain any peaks, showing the presence of an amorphous domain of inorganic component inside the NWs while sharp diffraction peaks one can observe in the medium angle region (1.5 – 30˚ 2θ), which indicate a high order degree (layered structures) of NWs (Figure 5).

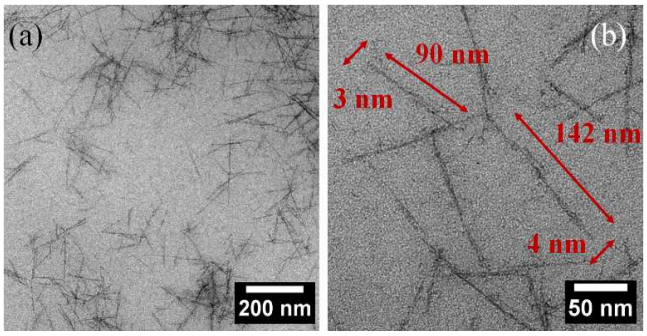

Figure 4. TEM images of NWs

Table 1 shows the diffraction data: 2θ values, Bragg distance (*d*), scattering vector[32] (Q) and Wave vectors ratio (Q_i / Q_1). One can see that the values of scattering vector's ratio ranged monotonous from 1.00 to 6.33, being in the string: 1:2:3:4:5:6.

Table 1. Powder X-ray diffraction data for NWs sample at room temperature.

Number of peak (i)	2è (°)	Bragg distance *d* (Å)	Scattering vector Q ($Å^{-1}$)	Ratio of scattering vectors, Q_i / Q_1
1	2.32	41.62	0.151	1.00
2	4.60	20.06	0.313	2.07
3	6.79	13.40	0.469	3.11
4	9.07	9.96	0.631	4.18
5	11.79	7.63	0.824	5.45
6	13.64	6.58	0.955	6.33

This kind of array of values was observed by us previously[33] and describe layered highly ordered materials, namely smectic crystals, a midway between the hard solid-phase crystals and the fluid classic liquid crystalline phase.[34] We believe that a self-assembling process of iron oxide covered with oleic acid and dodecylamine took place.[33]

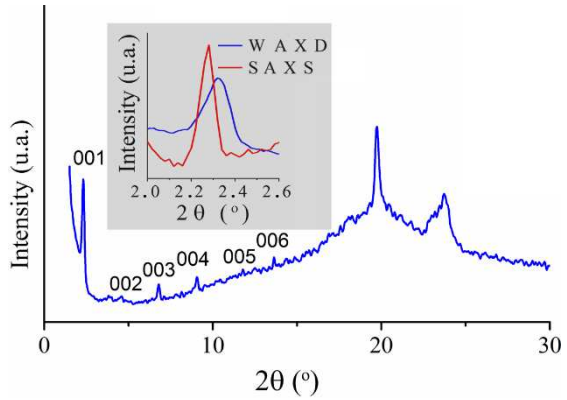

Figure 5. X-ray powder diffraction pattern of NWs in the medium angle region (1.5–30˚ 2θ) (inset: comparative WAXD and SAXS spectra in the range 2.0-3.0˚ 2θ).

The NWs sample in paste form was analysed by SAXS using a dedicated holder. The setup of the equipment allows the analysis in the range q= 0.006 $Å^{-1}$ - 0.15 $Å^{-1}$. Figure 6 shows the variation of the scattering intensity versus the scattering vector in logarithmic scale.

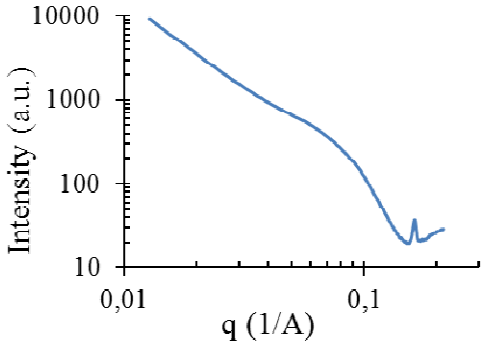

Figure 6. The scattering curve log(I) versus the scattering (spreading) vector, log(q).

The obtained graph presents a couple of characteristic elements that are useful for determination of the structural characteristics of the sample. The most important element of the scattering curve is concerned with the peak in the large q values region, near the detection limit of the device (Figure 6). The presence of this peak suggests that the elements in the system contain substructures arranged in an ordered manner that follows certain group symmetry. The correlation with the results from WAXD analysis (Figure 5 insert) confirms this supposition and indicates that this is a first order diffraction peak. The representation of the data in a correlated system of coordinates allowed us to identify the group symmetry as lammelar and the interlammelar distance was calculated: d= $2\pi/q_p$ = 6.1 nm.

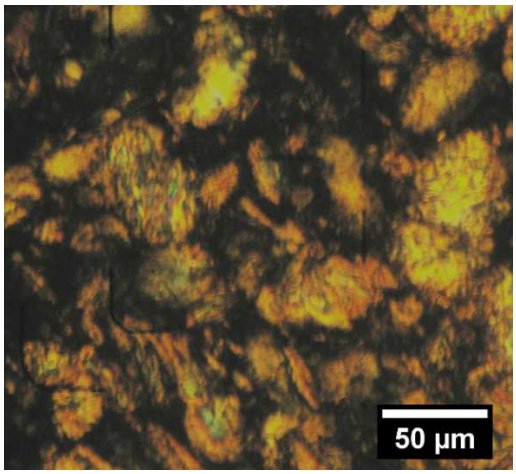

Figure 7. POM microphotograph showing birefringent texture of sample NWs at 22 oC.

The thermal behaviour of the NWs has been investigated by using both polarized optical microscopy (POM) and differential scanning calorimetry (DSC) measurements. Under POM at room temperature, the sample showed a birefringent texture (Figure 7) with irregular shape and shine, which could not be specifically assigned. We consider that is possible represents a poorly developed texture, as was similarly observed for unoriented twist grain boundary of smectic A phase (plates 41 and 111 in references [35]). At heating, the texture starts to flow around 40 ˚C and became an isotropic fluid at 65 ˚C. These transitions are also highlighted on DSC curves (Figure 8) showing an endothermic peak under heating at 58.4 °C together with an exothermal peak at 35.6 °C on the cooling run. These thermal transitions have been reproduced after three heating-cooling cycles, which demonstrated the morphological homogeneity of the sample. These confirm highly ordered nature of the material emphasized by XRD and SAXS techniques.

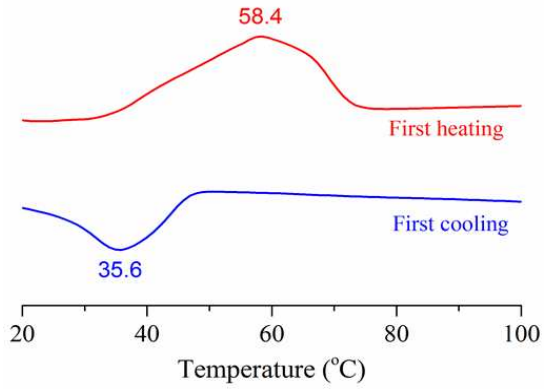

Figure 8. DSC traces of NWs

The Mössbauer spectra for NWs sample at various temperatures in the range of 7 – 293 K are shown in Figure 9 with pertinent parameters presented in Table 2. A strong doublet with moderate quadrupole splitting QS = 0.68 mm/s is observed at isomer shift IS = 0.40 mm/s at room temperature. Only minor traces of a sextet are present (fitted to < 9%) and are close to the noise level. This picture is constant down to 130 K, but from 115 K the area of sextets increases sharply so that at 110 K the sextet state is dominant. At 80 K, only a minor trace of a doublet can be observed and it fully disappears at 7 K. The non-degenerated state was fitted with two sextets to give reasonable χ^2_{red}, while the use of three sextets results in reduction of χ^2_{red} by only 0.05 units (for MS spectrum at 7 K). Both sextets at 7 K show similar isomer shift IS = 0.49, while the QS is -0.16 and -0.27 mm/s with internal hyperfine field H_{int} = 481 and 460 kG, respectively.

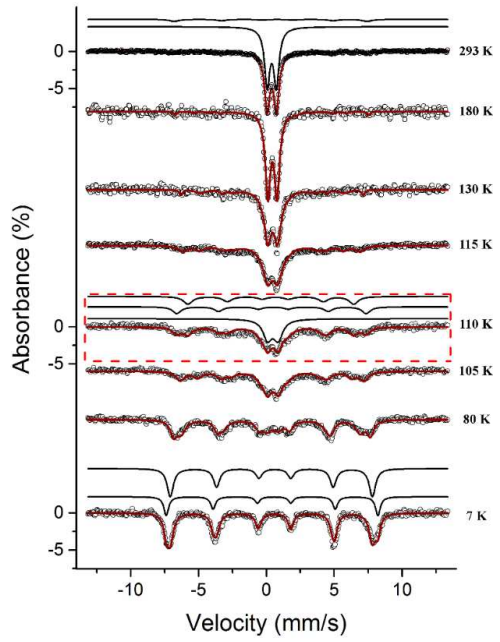

Figure 9. The Mössbauer spectra for NM17 over 7 – 293 K temperature range. The red square shows the closest to blocking temperature Mössbauer absorption pattern.

Table 2. Mossbauer parametres of NWs

Temperature, K	Isomer Shift*, δ, mm/s	Quadrupole Splitting*, ΔE_Q, mm/s	Hyperfine Field, H_{int}, kG	Full width at half maximum Γ, mm/s
RT	0.40	0.68	-	0.46
7 K	0.49	-0.16	481	0.41
	0.49	-0.27	460	0.54

* the error for values of IS and QS is ±0.02 mm/s.

The shape of the MS, their variation with temperature and the obtained parameters are characteristic for NPs of iron oxides and may be interpreted in the terms of superparamagnetic phenomenon. The blocking temperature represents, in general terms, the temperature at which the Néel relaxation time τ_N required for a nanoparticle magnetization to flip is equal to the measurement time τ_m. The Figure 10 shows the plot of doublet and summed sextets areas vs temperature. It is clearly seen that in temperature range of 110-115 K, the areas of doublet and summed sextets become equal, and from the crossing point of the two trend lines the blocking temperature was estimated to be about 111 K.

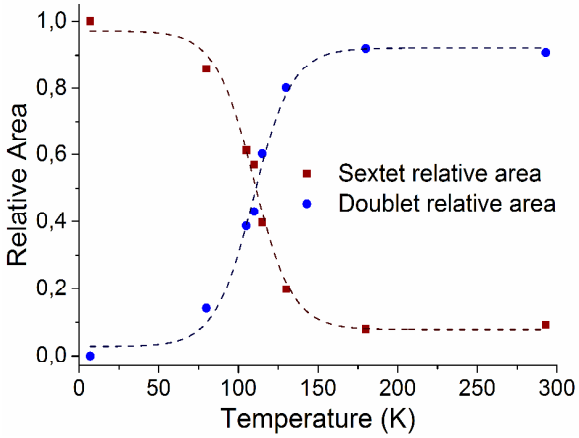

Figure 10. The plot of doublet (●) and summed sextets (■) areas vs temperature. The line is showing the sigmoidal trend of data fitted by Boltzmann function.

The residue of the thermogravimetrical analysis of the NWs was investigated by TEM (Figure 11a, b) and Raman spectroscopy (Figure S2). It could be observed that particles with various morphologies were formed: 20 nm nanoparticles with irregular shape and nanotubes with various sizes (length 100 – 900 nm; wide 25 – 40 nm). The metallic nature of nanotubes was highlighted using STEM (Figure 11 c). The peaks (377, 486, 670 and 717 cm^{-1}) found in Raman spectrum are characteristic for γ-Fe_2O_3 (maghemite)[31].

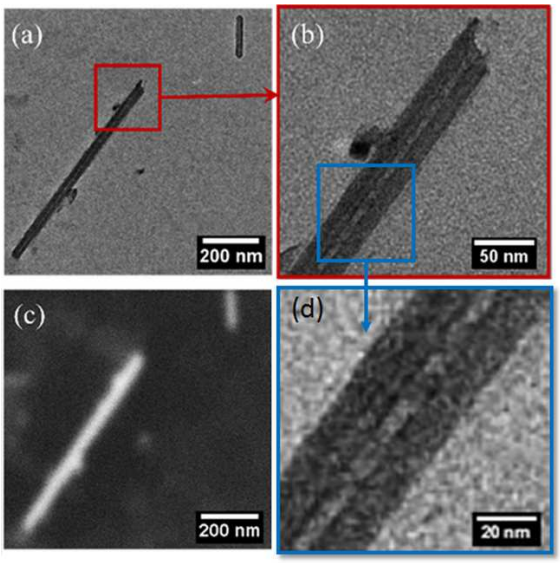

Figure 11. TEM images (a,b,d) and STEM image (d) of NWs heated at 700 oC in nitrogen atmosphere (TGA residue)

The magnetic properties of the sample were measured in dc-magnetic field up to 7 T and in the temperature range of 5-300 K (Figure 12). The temperature dependence of magnetization measured in ZFC (zero-field cooling) and FC (field cooling) regimes in external magnetic field of 10 Oe (1mT) shows the irreversibility of both curves below the temperature of Tirr ~ 120 K. Paramagnetic-like temperature dependence of magnetization with merged ZFC and FC curves was observed above Tirr. Such behaviour suggests the existence of superparamagnetic state in the sample, despite the absence of a typical maximum in ZFC magnetization curve. To identify the blocking temperature TB of NW magnetic moments we used the procedure reported by Denardin et al.[36].(Figure 12b). The value of TB ~ 115 K estimated from SQUID measurements is comparable to that obtained from Mössbauer spectroscopy. The existence of blocking process of magnetic moments in studied sample was confirmed also from field dependence of magnetization at various temperatures, Figure 12c,d. Magnetization curve at room temperature exhibits the typical paramagnetic feature. The value of magnetic moment of superparamagnetic particles mp ~ 38μB was obtained from the fit of experimental data by the Langevin function[37] at 300 K. This value is lower than reported magnetic moments in various iron oxide nanoparticles[37,38], and could explain the absence of maximum in ZFC curve. The magnetization curve measured at 5 K (Figure 12d) exhibits the hysteresis, with weak coercivity of HC ~ 140 Oe and confirms the ferromagnetic interactions due to the blocking process below TB. With decreasing temperature from 300 K to 5 K the saturation magnetization value increases from 0.30 emu/g to 4.12 emu/g, see Figure 12e. Such behaviour was observed also on various iron oxide nano-systems[38–40] and is related to thermal fluctuations of nanoparticle magnetic moments through an energy barrier. In comparison with other iron oxide nanoparticles, we observed the unsaturated hysteresis loops and also the increase of magnetization with decreasing temperature is more pronounced. We assume that this could be due to the higher surface area and anisotropic morphology of the nanowire. In the case of superparamagnetic particles with uniaxial anisotropy the blocking temperature TB is related to the anisotropy constant K by equation[39,41] TB = KV V/25kB, where V is the volume. The value of anisotropy constant in studied sample was calculated to be 56 kJ/m3. The obtained value is higher than the anisotropy constant of bulk maghemite (5–15 kJ/m3) due to the nanosize effect, but comparable with other maghemite nanosystems.[39]

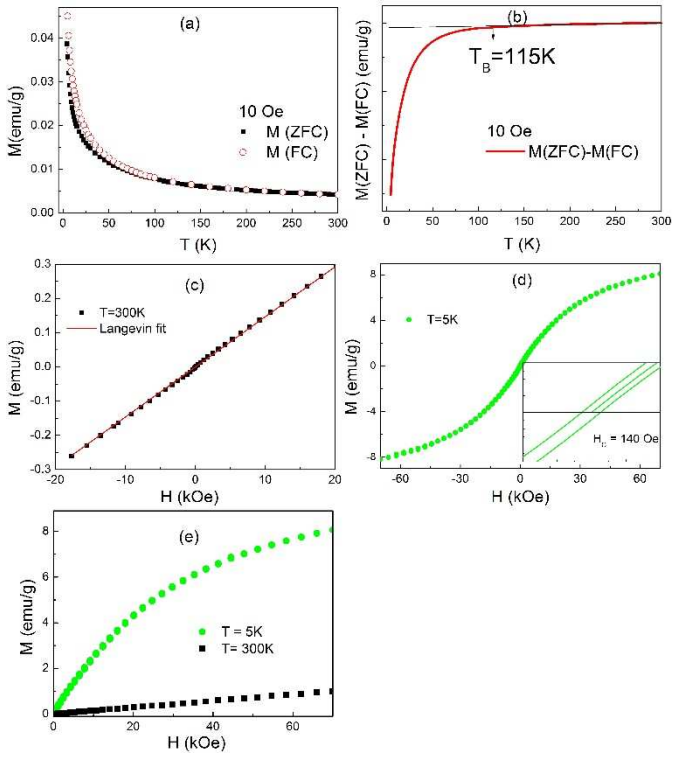

Figure 12. Magnetic measurements of studied compound: (a) the magnetization of the sample, measured in ZFC and FC regimes, in the magnetic field of 1 mT (10 Oe); (b) difference between ZFC and FC magnetization with marked TB point; (c) the hysteresis loops of the sample at 300 K including Langevin fit of experimental data; (d) the hysteresis loops of the sample at 5 K, (e) comparison of M vs. H at different temperatures.

Experimental

Materials

μ3-oxo trinuclear iron(III) acetate ($[Fe_3O(CH_3COO)_6(H_2O)_3]NO_3 \cdot 4H_2O$), IA, was obtained by a known procedure[42] using as reagents $Fe(NO_3)_3 \cdot 9H_2O$ and CH_3COONa, glacial acetic acid and distilled water. The structure of the compound was confirmed by FTIR (ν_{max} (KBr), cm^{-1}: 420vw, 468vw, 527w , 613s, 662s, 822w, 835w, 898vw, 951w, 1035m, 1292s, 1385vs, 1450vs, 1589vs, 1688s, 2545vw, 2636vw, 3413s) and single crystal XRD (literature[42]: a = 15.69(3), b = 11.77(2), c = 15.32(4) Å); obtained: a = 15.65, b =

11.765, c = 15.31 Å). Dodecylamine (Fluka), Oleic acid (Sigma-Aldrich) and Trichloroacetic acid (Fluka) were used as received without any purification process.

Equipment

Fourier transform infrared (FTIR) spectra were recorded with a Bruker Vertex 70 FTIR spectrometer in transmission mode with collection of 32 scans, in the range 400-4000 cm^{-1}, at room temperature, with a resolution of 2 cm^{-1}. Samples were incorporated as dried powder in KBr pellets. For identifying the phases in powder was used *Wide Angle X-rays Diffraction (WAXD)* analysis performed on a Bruker-AXS D8 ADVANCE diffractometer, with Bragg Brentano parafocusing goniometer. Scans were recorded in step mode using Ni-filtered Cu K! radiation λ = 0.1541 nm). The working conditions were 40 kV and 30 mA tube power. The Bruker computer softwares Eva 11 and Topaz 3.1 were used to plot and process the data. *Small Angle X-ray Scattering (SAXS)* was used to characterize the nanometric structure of the powdered sample phase. Data was collected at the Bruker-Nanostar U apparatus equipped with a 3-pinhole collimation system that provides a precisely parallel X-ray beam with high intensity and virtually no background so that fast measuring times and extremely high resolution can be achieved. The scattering intensity was measured as a function of scattering vector, q, being defined as $q = (4\pi/\lambda)\sin\theta$, where 2θ is the scattering angle and λ is the X-ray wavelength (1.54 Å). The space group has been determined using SGI (space group indexing) software. *Thermogravimetric analysis (TGA)* was performed on a Mettler Toledo TGA-SDTA851e type derivatograph (thermogravimetric analyzer) under nitrogen flow (20 ml/min), within 25-1000°C range, at 10°C·min^{-1} heating rate for samples of 2-5 mg each. Alumina crucibles (70 µl) were used as sample holders. Every experiment was repeated three times and showed a good reproducibility. The data were processed using the STAR software Mettler Toledo. *DSC measurements* were conducted with a DSC 200 F3 Maia (Netzsch, Germany). About 9 mg of sample was heated in pressed and punched aluminium crucibles at a heating rate of 10 ºC min^{-1}. Nitrogen was used as inert atmosphere at a flow rate of 100 mL min^{-1}. *The Transmission Electron Microscopy (TEM)* images were taken using a dedicated HITACHI HT7700 microscope specifically dedicated to soft materials operating in high contrast mode at 100 kV accelerating voltage. The samples have been prepared by placing small droplets of the diluted dispersion (~1g/L) of iron oxide nanoparticles on 300 mesh carbon coated copper grids and dried in vacuum at 50 ºC. *The Mössbauer spectra* were acquired using a conventional spectrometer in the constant-acceleration mode (MS4, Edina,USA) equipped with a ^{57}Co source (3.7 GBq) in a rhodium matrix. Isomer shifts are given relative to α-Fe at room temperature. The samples were measured in the temperature range 6.5 – 300 K and the spectra were fitted using the WMOSS Mössbauer Fitting Program (Edina). *Magnetic measurements* were performed in MPMS3 SQUID-based magnetometer (Quantum Design) in the temperature range 5-300 K. Powdered sample was held in gelatine capsule and the background signal of the capsule was subtracted from the total magnetization.

Preparation of iron oxide nanowires (NWs)

A mixture consisting in IA (1 g), dodecylamine (5 g), oleic acid (2.9 ml) and thricloroacetic acid (6.3 g) was introduced in a three-necked flask equipped with condenser, thermometer and heating mantle and was slowly heated till 320˚C, being maintained for 30 min at this temperature. Then, the mixture was gradually cooled at room temperature, after that this was dispersed in hexane and filtered. Ethanol was added to the filtrate mixture and it was then centrifuged. This purification protocol was repeated 3 times. After drying, a product with viscous appearance was obtained. IR (KBr), ν(cm^{-1}) = 393m, 411m, 490vw, 665m, 719m, 864w, 964w, 1045vw, 1092vw, 1161vw, 1230vw, 1375w, 1466m, 1549m, 1636s, 1705w, 1740vw, 2353vw, 2450vw, 2533vw, 2450vw, 2530vw, 2783vw, 2853vs, 2922vs, 2955s, 3317w, 3385w.

Conclusions

Iron oxide nanowires stabilized with oleic acid - dodecilamine mixture have been obtained by a simple optimized procedure. This morphology was emphasized by TEM. Powder WAXD measurements indicated a high order degree of the nanoparticles, namely smectic crystals, but also the presence of amorphous domain of inorganic component within them. The liquid crystalline phase was also confirmed by SAXS, DSC and POM. The material is thermally stable up to around 205 ˚C. The MS data are characteristic for NPs of iron oxides and may be interpreted in the terms of superparamagnetism phenomenon, the estimated blocking temperature being at about 111 K. After thermal decomposition in the conditions of thermogravimetrical analysis γ-Fe_2O_3 (maghemite) nanotubes with various size resulted. Magnetic behaviour of studied system is in a good agreement with MS results and confirm the existence of blocking process of NW magnetic moments below T_B ~ 115 K. Above this temperature, the magnetic moments freely fluctuate across to energy barrier and system exhibits the paramagnetic properties. We assume that due to the high surface area and anisotropy morphology in combination with known biocompatibility and low cytotoxicity of their components, the prepared iron oxide nanowires can be used as T_2 contrast agents.

Acknowledgements

This work was supported by a grant of the Ministry of National Education, CNCS – UEFISCDI, project number PN-II-ID-PCE-2012-4-0261 (Contract 53/2013), by the Slovak Research and Development Agency under the contact no. APVV-0132-11 and the Slovak Grant Agency VEGA 1/0145/13.

Notes and references

[a]"Petru Poni" Institute of Macromolecular Chemistry, Iasi, 700487, Romania; mcazacu@icmpp.ro.
[b]Institute of Chemistry of ASM, Academiei str. 3, Chisinau 2028, Republic of Moldova;
[c]Institute of Physics, Faculty of Science, P. J. Šafárik University, Park Angelinum 9, 04154 Košice, Slovakia

Electronic Supplementary Information (ESI) available: X-ray powder diffraction pattern (30–70° 2θ) of NWs and Raman spectrum of calcinated NWs. See DOI: 10.1039/x0xx00000x

1 S. Laurent, D. Forge, M. Port, A. Roch, C. Robic, L. Vander Elst and R. N. Muller, *Chem. Rev.*, 2008, **108**, 2064–110.
2 M. Mahmoudi, S. Sant, B. Wang, S. Laurent and T. Sen, *Adv. Drug Deliv. Rev.*, **63**, 24–46.
3 D. Chen, S. Xiong, S. Ran, B. Liu, L. Wang and G. Shen, *Sci. China Physics, Mech. Astron.*, 2011, **54**, 1190–1199.
4 J. Wang, M. S. Gudiksen, X. Duan, Y. Cui and C. M. Lieber, *Science*, 2001, **293**, 1455–7.
5 H. Kind, H. Yan, B. Messer, M. Law and P. Yang, *Adv. Mater.*, 2002, **14**, 158–160.
6 S. P. Rwei, L. Y. Wang and M. J. Chen, *J. Nanomater.*, 2013, **2013**, 1–8.
7 W.-S. Lin, Z.-J. Jian, H.-M. Lin, L.-C. Lai, W.-A. Chiou, Y.-K. Hwu, S.-H. Wu, W.-C. Chen and Y. D. Yao, *J. Chinese Chem. Soc.*, 2013, **60**, 85–91.
8 L. M. Armijo, Y. I. Brandt, D. Mathew, S. Yadav, S. Maestas, A. C. Rivera, N. C. Cook, N. J. Withers, G. A. Smolyakov, N. L. Adolphi, T. C. Monson, D. L. Huber, H. D. C. Smyth and M. Osiński, *Nanomaterials*, 2012, **2**, 134–146.
9 K. C.-F. Leung, Y.-X. J. Wang, H. Wang, S. Xuan, C.-P. Chak and C. H. K. Cheng, *IEEE Trans. Nanobioscience*, 2009, **8**, 192–8.
10 J. Wu, L. Liu, S. Liu, P. Yu, Z. Zheng, M. Shafa, Z. Zhou, H. Li, H. Ji and Z. M. Wang, *Nano Lett.*, 2014, **14**, 6002–9.
11 Y. A. Gorby, S. Yanina, J. S. McLean, K. M. Rosso, D. Moyles, A. Dohnalkova, T. J. Beveridge, I. S. Chang, B. H. Kim, K. S. Kim, D. E. Culley, S. B. Reed, M. F. Romine, D. A. Saffarini, E. A. Hill, L. Shi, D. A. Elias, D. W. Kennedy, G. Pinchuk, K. Watanabe, S. Ishii, B. Logan, K. H. Nealson and J. K. Fredrickson, *Proc. Natl. Acad. Sci. U. S. A.*, 2006, **103**, 11358–63.
12 T. Adam and H. U, *Curr. Nanosci.*, 2014, **10**, 695–699.
13 J. Mohapatra, A. Mitra, H. Tyagi, D. Bahadur and M. Aslam, *Nanoscale*, 2015.
14 M. Bengtsson, K. Oksman and N. M. Stark, *Polym. Compos.*, 2006, **27**, 184–194.
15 Y. Fu, J. Chen and H. Zhang, *Chem. Phys. Lett.*, 2001, **350**, 491–494.
16 G. Wang, X. Gou, J. Horvat and J. Park, *J. Phys. Chem. C*, 2008, **112**, 15220–15225.
17 M. Pregelj, P. Umek, B. Drolc, B. Jančar, Z. Jagličič, R. Dominko and D. Arčon, *J. Mater. Res.*, 2011, **21**, 2955–2962.
18 H. W. Kim, S. H. Shim, B. H. O, S. G. Lee, S. G. Park and E. H. Lee, in *Key Engineering Materials*, 2007, vol. 342-343, pp. 597–600.
19 L. Suber, P. Imperatori, G. Ausanio, F. Fabbri and H. Hofmeister, *J. Phys. Chem. B*, 2005, **109**, 7103–9.
20 S. Mollah, S. Henley, C. Giusca and S. Silva, *Integr. Ferroelectr.*, 2010.
21 J. Park, K. An, Y. Hwang, J.-G. Park, H.-J. Noh, J.-Y. Kim, J.-H. Park, N.-M. Hwang and T. Hyeon, *Nat. Mater.*, 2004, **3**, 891–5.
22 M. Zhong, Z. Liu, X. Zhong, H. Yu and D. Zeng, *J. Mater. Sci. Technol.*, 2011, **27**, 985–990.
23 A. Valor, E. Reguera, E. Torres-García, S. Mendoza and F. Sanchez-Sinencio, *Thermochim. Acta*, 2002, **389**, 133–139.
24 W. W. Yu, J. C. Falkner, C. T. Yavuz and V. L. Colvin, *Chem. Commun. (Camb).*, 2004, 2306–7.
25 Y. Bao, W. An, C. H. Turner and K. M. Krishnan, *Langmuir*, 2010, **26**, 478–83.
26 A. R. Roosen and W. C. Carter, *Phys. A Stat. Mech. its Appl.*, 1998, **261**, 232–247.
27 K.-S. Cho, D. V Talapin, W. Gaschler and C. B. Murray, *J. Am. Chem. Soc.*, 2005, **127**, 7140–7.
28 B. Wiley, Y. Sun, B. Mayers and Y. Xia, *Chemistry*, 2005, **11**, 454–63.
29 A. L. Willis, N. J. Turro and S. O'Brien, *Chem. Mater.*, 2005, **17**, 5970–5975.
30 K. Nakamoto, *Infrared and Raman Spectra of Inorganic and Coordination Compounds*, John Wiley & Sons, 1986, vol. 85.
31 R. M. Cornell and U. Schwertmann, *The Iron Oxides: Structure, Properties, Reactions, Occurences and Uses, Second Edition*, Wiley-VCH, Weinheim, Wiley-VCH., 2004.
32 J. M. Seddon, in *Handbook of Liquid Crystals Set*, eds. D. Demus, J. Goodby, G. W. Gray, H.-W. Spiess and V. Vill, Wiley-VCH Verlag GmbH, Weinheim, Germany, 1998, pp. 635–679.
33 M. Iacob, M. Cazacu, C. Racles, M. Ignat, V. Cozan, L. Sacarescu, D. Timpu, M. Kajňaková, M. Botko, A. Feher and C. Turta, *RSC Adv.*, 2014, **4**, 6293.
34 A. Garcia-Márquez, A. Demortière, B. Heinrich, D. Guillon, S. Bégin-Colin and B. Donnio, *J. Mater. Chem.*, 2011, **21**, 8994.
35 I. Dierking, *Textures of Liquid Crystals*, Wiley-VCH Verlag GmbH & Co, Weinheim, 2003.
36 J. C. Denardin, A. L. Brandl, M. Knobel, P. Panissod, A. B. Pakhomov, H. Liu and X. X. Zhang, *Phys. Rev. B*, 2002, **65**, 064422.
37 T. M, K. S, J. M, H. D and M. D, *Appl. Surf. Sci.*, 2014, **322**, 255–264.
38 J. Tucek, R. Zboril and D. Petridis, *J. Nanosci. Nanotechnol.*, 2006, **6**, 926–47.
39 A. Espinosa, A. Muñoz-Noval, M. García-Hernández, A. Serrano, J. Jiménez de la Morena, A. Figuerola, A. Quarta, T. Pellegrino, C. Wilhelm and M. A. García, *J. Nanoparticle Res.*, 2013, **15**, 1514.
40 D. Vollath, D. V. Szabó, R. D. Taylor, J. O. Willis and K. E. Sickafus, *Nanostructured Mater.*, 1995, **6**, 941–944.
41 S. P. Gubin, Y. A. Koksharov, G. B. Khomutov and G. Y. Yurkov, *Russ. Chem. Rev.*, 2005, **74**, 489–520.
42 K. I. Turte, S. G. Shova, F. A. Spatar, M. D. Mazus and T. I. Malinovskii, *J. Struct. Chem.*, 1994, **35**, 248–255.

